Time lag correction

Accurate temporal alignment between the vertical wind speed and particle concentration signals is essential for reliable flux calculations. Since the AIMMS-20 probe and the isokinetic inlet are located at different positions on the aircraft, a time lag exists between the two signals. Lag times were determined individually for each flux calculation period using covariance maximization, as described in Section 2.3.2 of the main text. This section provides the supporting validation analysis.

CPC synchronization validation

Both CPCs draw sample air from the same isokinetic inlet manifold. However, because each CPC detector unit is connected to the manifold via tubing of different length, the air transport time from the inlet to each detector differs (Fig. 4, Goldberger, 2020). This difference in transport time means the two CPCs may not sample identical air parcels at exactly the same moment, necessitating validation of their temporal synchronization. Figure S1 shows concentration measurements from both CPCs for a representative flight day. Despite differing absolute values, expected given their different size detection limits (3 nm vs. 10 nm), the temporal patterns closely align. To quantify this agreement, Spearman correlation coefficients (ρ) were calculated for both CPC records after removing cloud droplet shattering artifacts and excluding SPE periods, since only the ultrafine CPC detects SPEs. From the complete campaign dataset, 370 seconds of data were randomly selected to avoid selection bias, yielding a mean ρ of 0.97 (Fig. S2).The full CPC dataset was segmented into 20-second intervals, each corresponding to approximately 2 km of horizontal flight path, and lag times were determined for each interval using covariance maximization (Fig. S3). Lag times of 0 and 1 seconds occurred in 13% and 27% of intervals respectively. The variability in lag times arises primarily from the 1 Hz temporal resolution of the measurements: since the true lag is unlikely to be an exact integer number of seconds, it is effectively rounded to the nearest second when determined by covariance maximization, causing an apparent alternation between 0 and 1 second values. Secondary contributions may arise from minor variations in flow velocity within the inlet tubing due to changes in ambient pressure and temperature with altitude, despite active flow rate regulation. On the spatial scale, lag times of 0 and 1 seconds correspond to spatial displacements of 0–100 m at typical aircraft speeds, which is small relative to the flux-carrying eddy scales resolved in this study. No single lag time was sufficiently dominant to apply uniformly across the campaign; applying a uniform lag would therefore introduce systematic errors in the flux covariance. Sensitivity analysis confirmed that derived fluxes change by an average of less than 16% when the lag is varied by ±1 second, supporting the robustness of the individual lag determination approach.

Pressure-based lag time validation

The lag correction was independently validated by comparing pressure measured at the isokinetic inlet with static pressure measured by the Rosemount 1201F1 sensor on the AIMMS-20 probe. Since both sensors respond to the same ambient pressure field, they should be in close agreement if the instruments are sampling the same air mass. Figure S4 shows pressure time series from both sensors for a representative flight day, confirming that both records track the same pressure variations at 1 Hz resolution. Figure S5 shows the Spearman correlation coefficient between the two pressure records across the full campaign, yielding ρ = 0.99 with values closely following the 1:1 line, confirming that both instruments sampled the same air mass with negligible systematic offset. Covariance maximization applied to the pressure records (Figure S6) again showed that no single lag time was appropriate across the full campaign, consistent with the CPC-based analysis and further supporting the use of individually determined lag times for each flux calculation period.

.

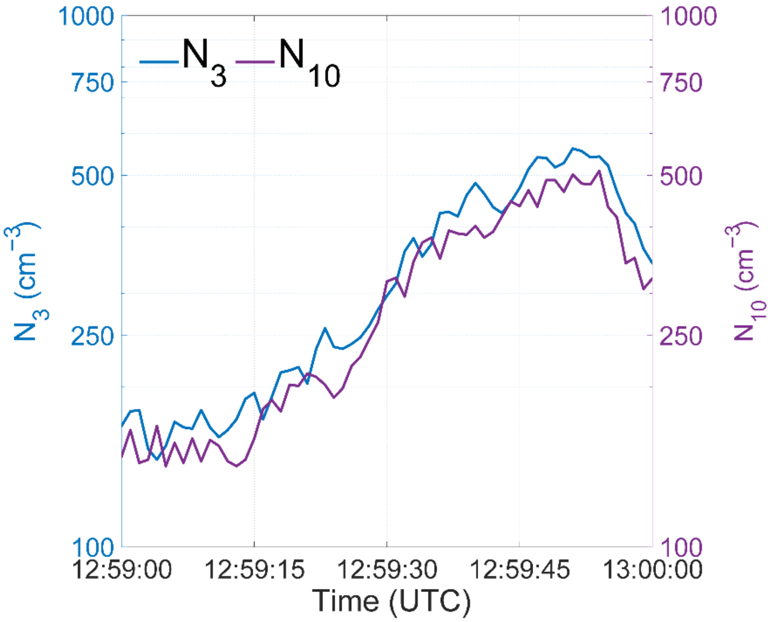

Figure S1. Time series of particle concentration measurements from both CPCs (CPC 3025A and CPC 3772) for a representative flight day, showing that the temporal patterns closely align despite differing absolute values due to different size detection limits.

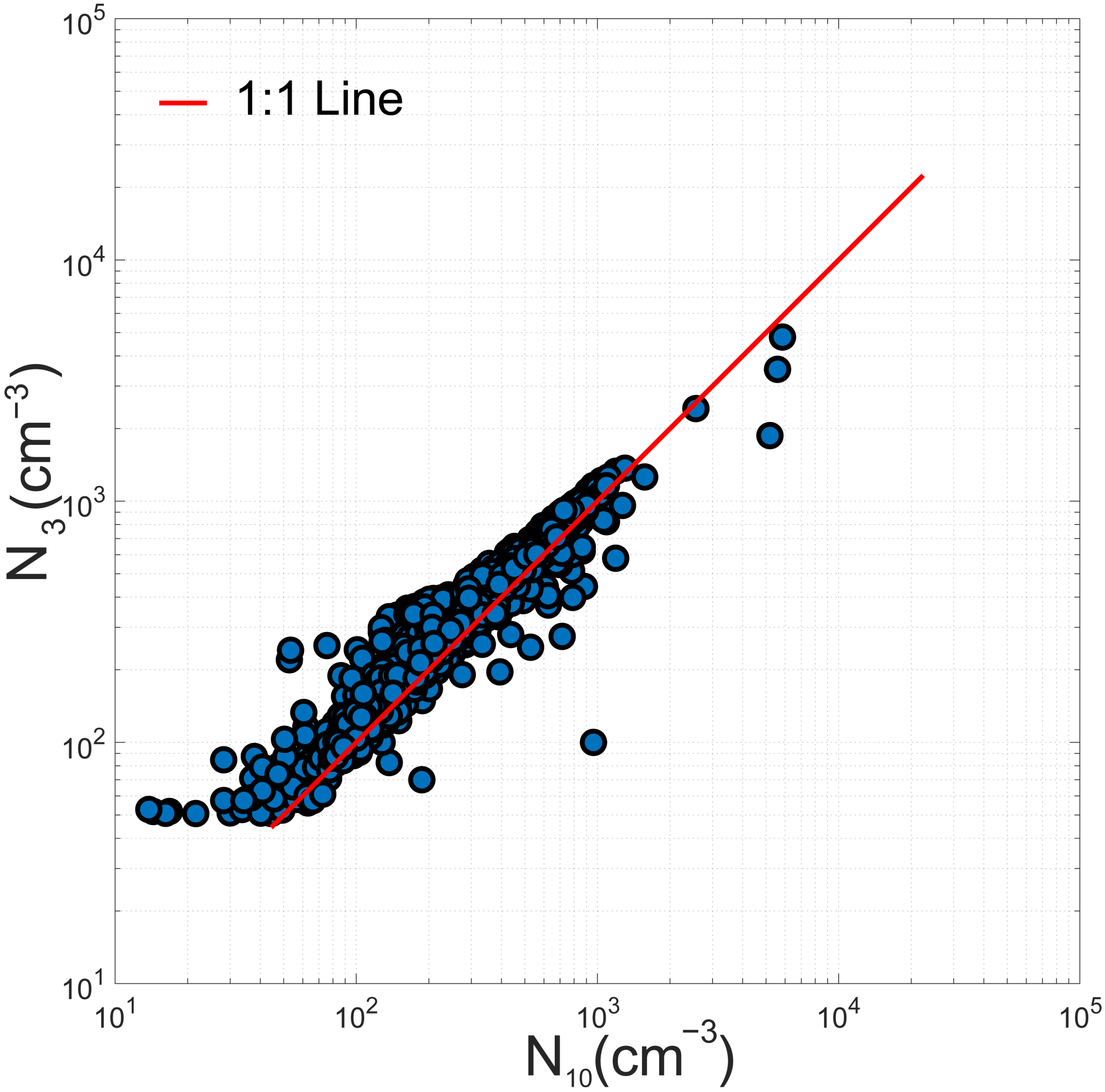

Figure S2. Spearman correlation coefficient analysis for the CPC concentration measurements, showing the distribution of correlation values from the 370 randomly selected seconds of data across the campaign, with the mean ρ = 0.97 indicated.

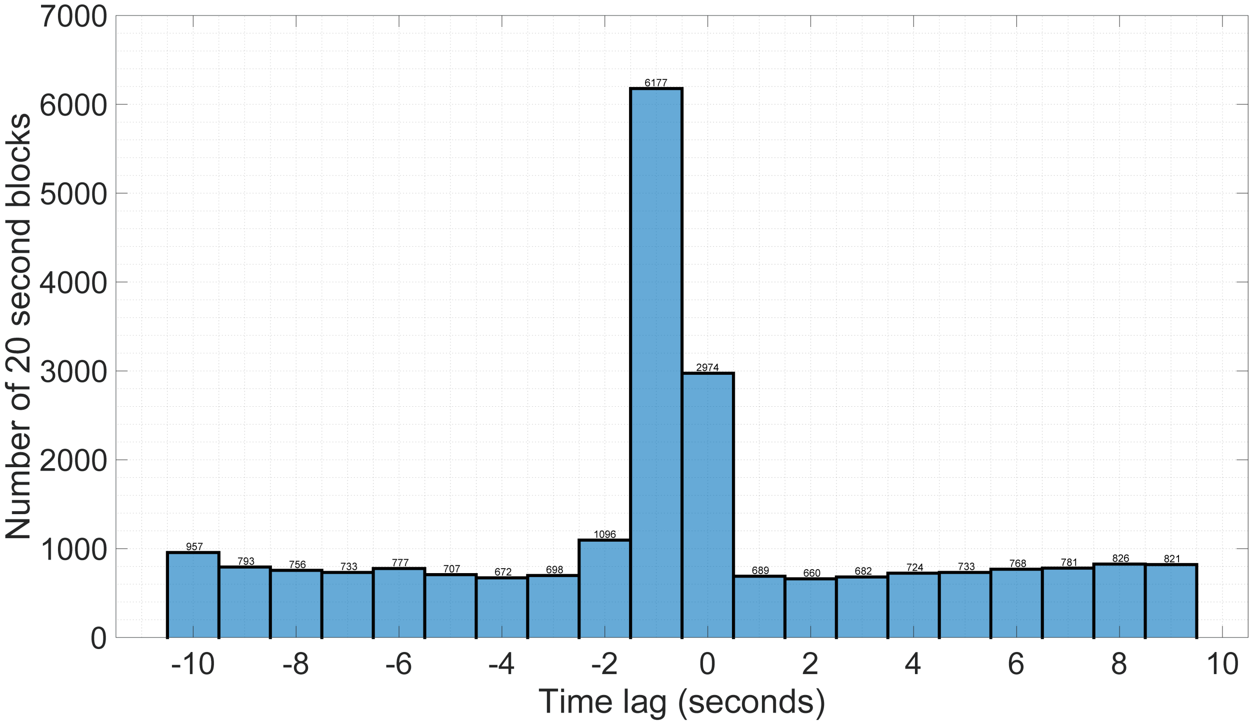

Figure S3. Distribution of lag times determined by covariance maximization across all 20-second flight segments for the entire campaign, showing that lag times of 0 and 1 seconds occurred in 13% and 27% of cases respectively, and demonstrating why no single fixed lag time was appropriate for the full campaign.

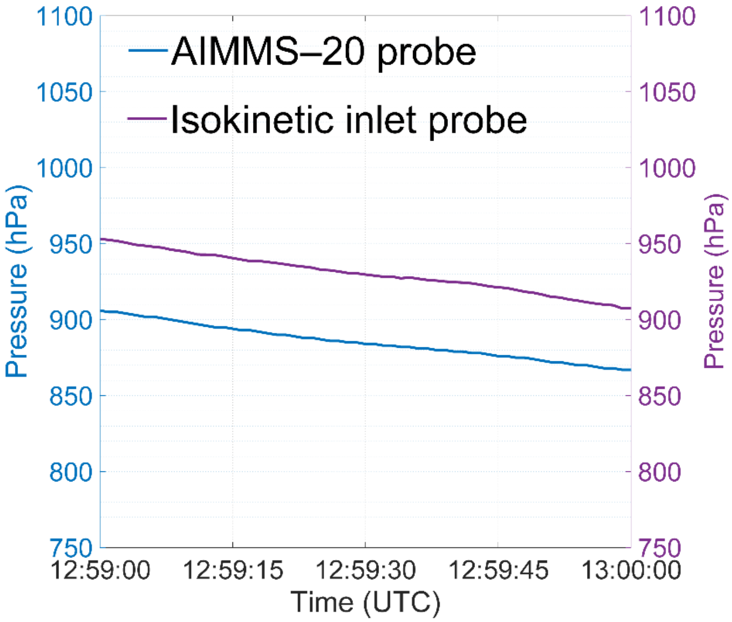

Figure S4. Time series of pressure measurements from the isokinetic inlet and the AIMMS-20 static pressure sensor for a representative flight day, demonstrating that both measurements follow similar pressure variation patterns at 1 Hz temporal resolution.

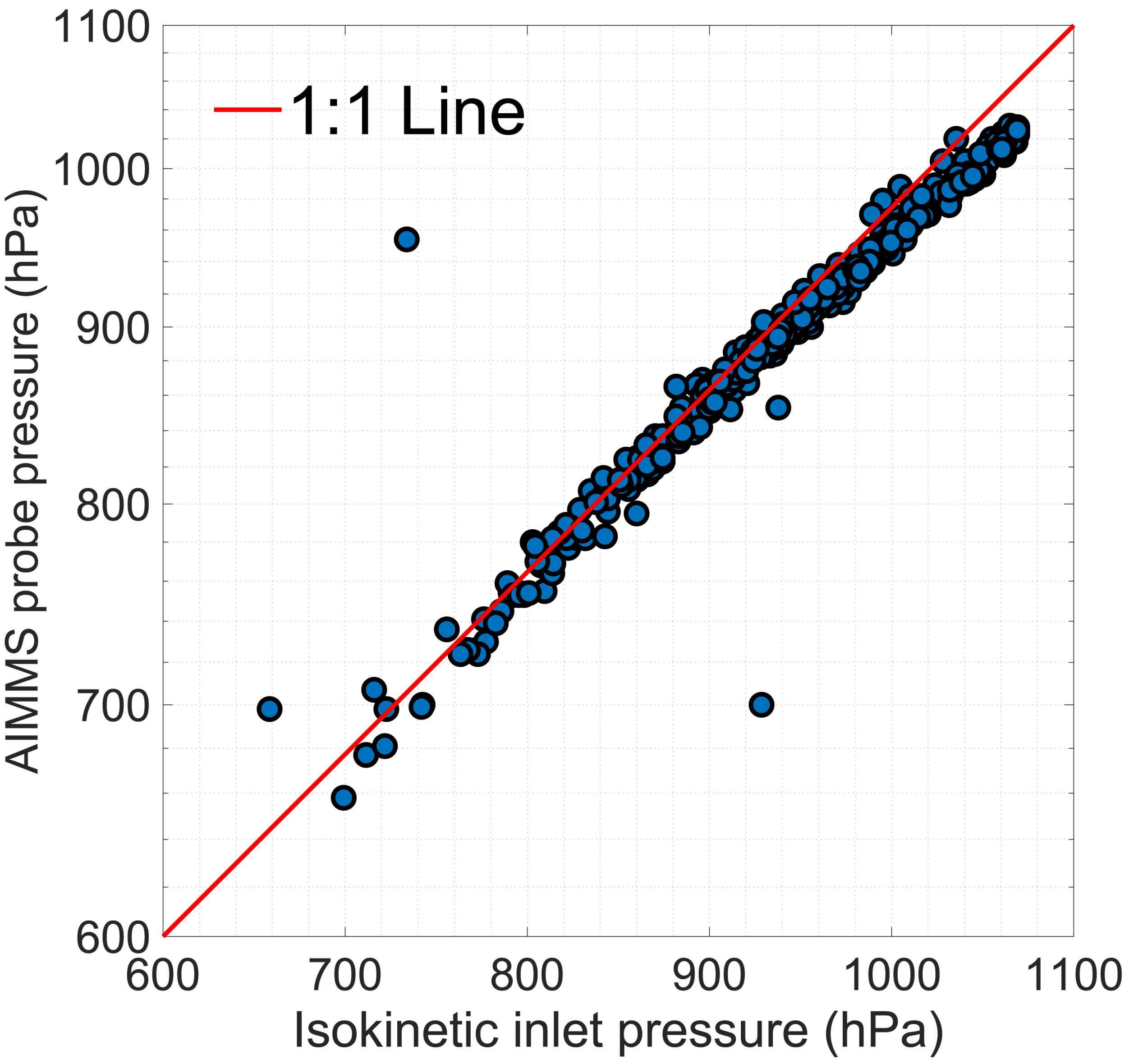

Figure S5. Scatter plot of pressure measurements from the Rosemount 1201F1 sensor attached to the AIMMS–20 probe vs those at the isokinetic inlet.

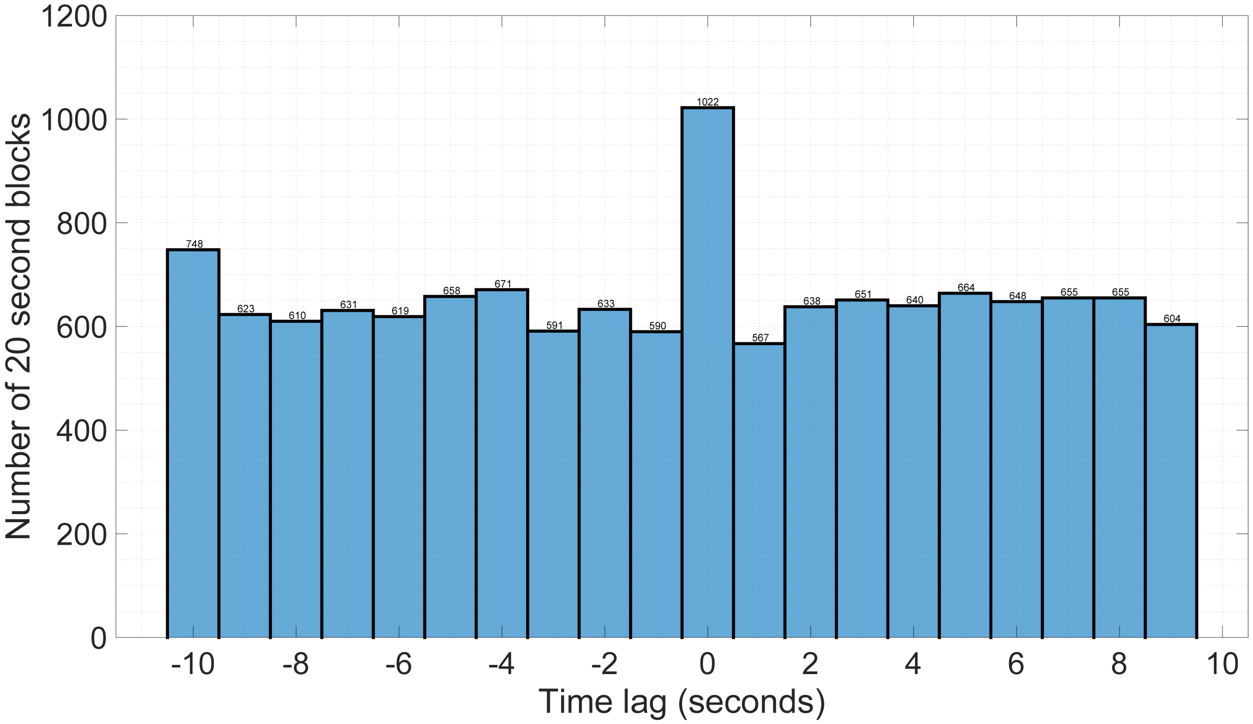

Figure S6. Frequency distribution of pressure-derived lag times across the campaign, showing consistency with the CPC-derived lag time analysis and supporting the individual lag time determination approach.

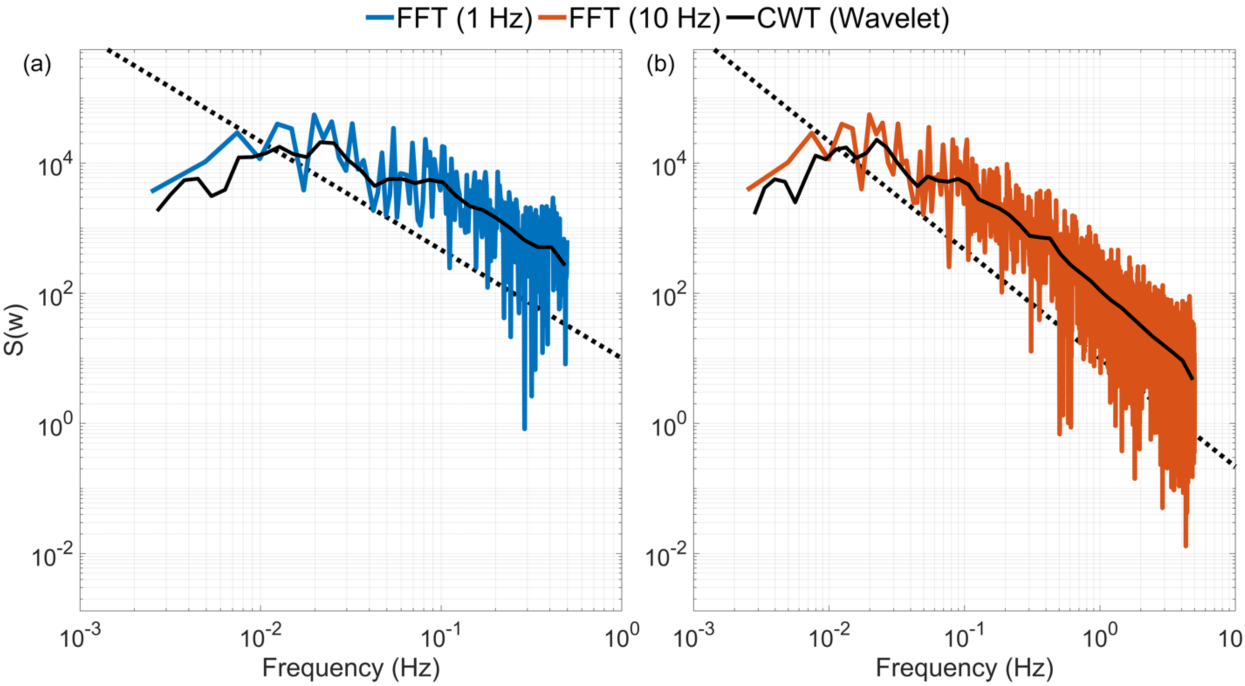

Figure S7. Power spectral density for vertical wind velocity at (a) 1 Hz and (b) 10 Hz

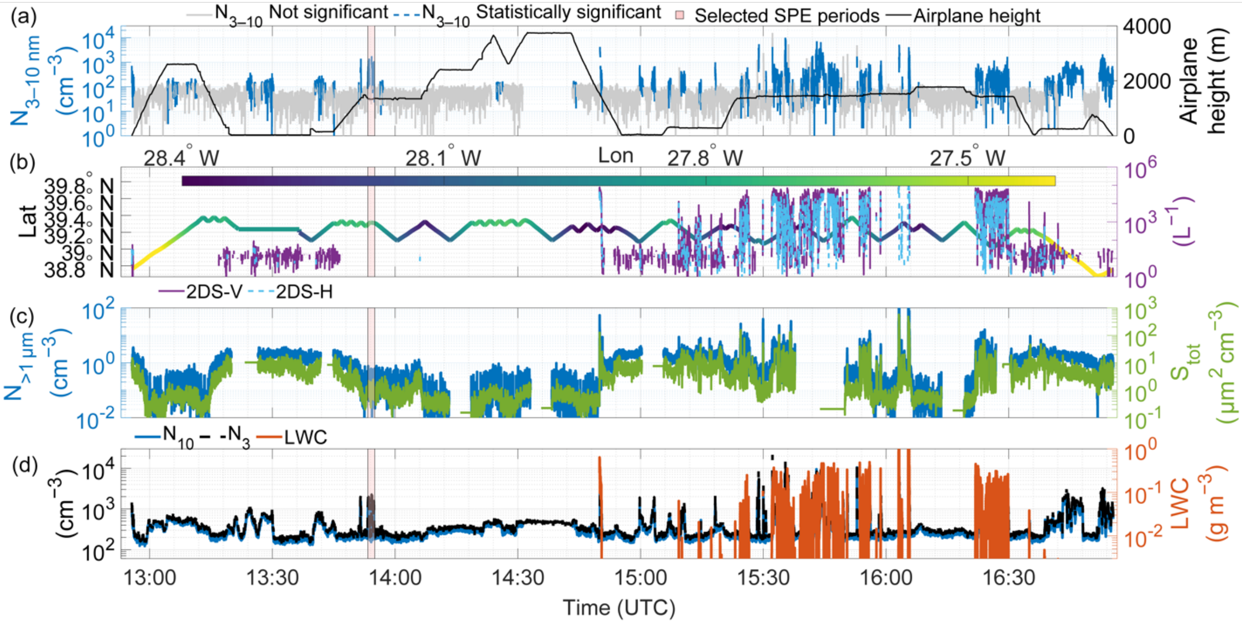

Figure S8. **Multi-parameter time series analysis during the February 10, 2018 flight showing: (a) $N_{3\text{-}10}$ particle concentrations and aircraft altitude; (b) aircraft position (latitude and longitude) and drizzle number concentration; (c) supermicron particle concentration and total particle surface area (S_{tot}) (d) particle number concentrations (N_{10} and N_3) and liquid water content. Gaps in the time series indicate the missing data.**

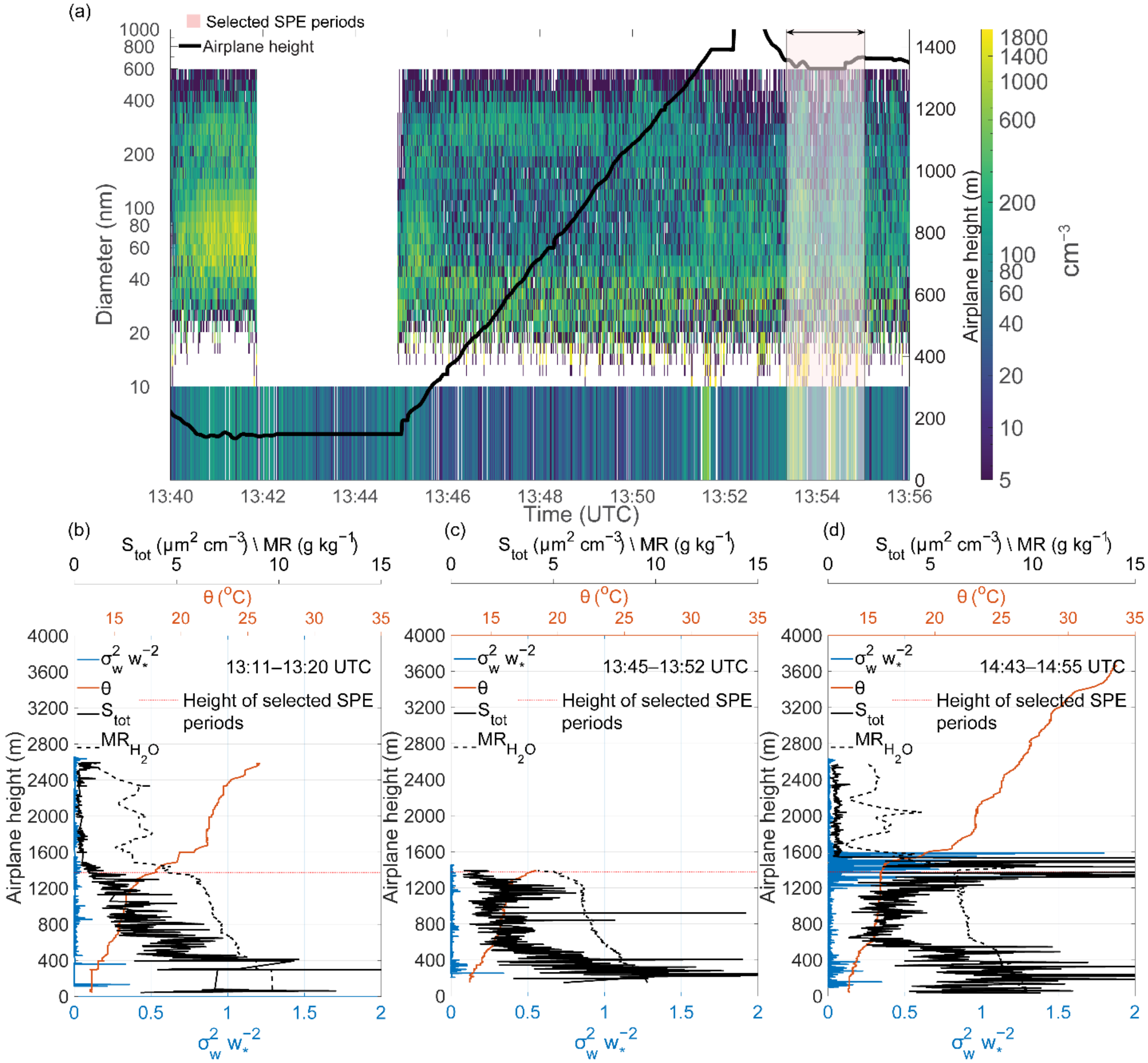

Figure S9. (a) Size-resolved particle number concentrations (10–600 nm) from FIMS as a function of time and altitude, with $N_{3\text{–}10}$ concentrations shown in the lower strip. Pink shading indicates selected SPE periods. (b-d) Vertical profiles of potential temperature (θ), normalized vertical velocity variance ($\sigma_w^2\, w_*^{-2}$), total particle surface area (S_{tot}), and water vapor mixing ratio (MR_{H_2O}) for three time periods nearest to the selected SPE periods: (b) 13:11–13:20 UTC, (c) 13:45–13:52 UTC, and (d) 14:43–14:55 UTC. Gaps in the time series indicate the missing data.

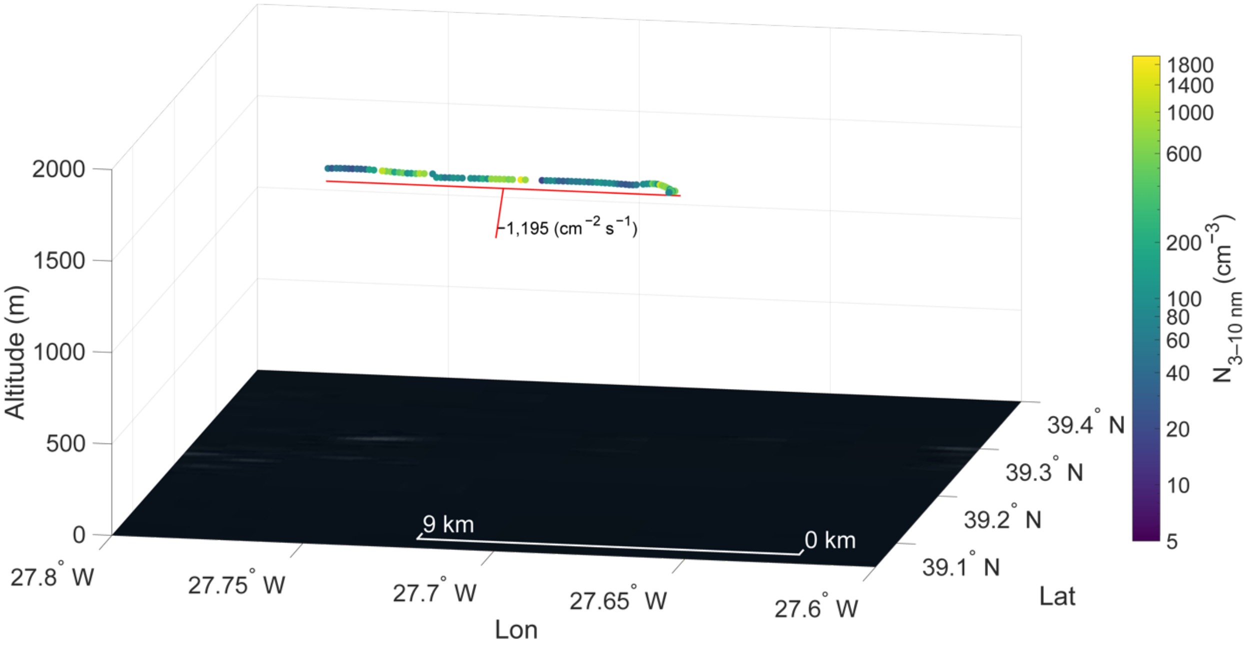

Figure S10. Spatial distribution of $N_{3\text{-}10}$ particle concentrations along the flight track at ~1375 m altitude during the period highlighted in Figures S8 and S9. Calculated vertical turbulent fluxes are labeled at their respective measurement locations. Color scale indicates $N_{3–10}$ particle number concentrations (cm^{-3}). The background shows a true-color satellite-corrected reflectance image from the overpass at 14:25 UTC, with the ocean surface appearing dark and clouds appearing white, Credit: NASA Worldview Snapshots.

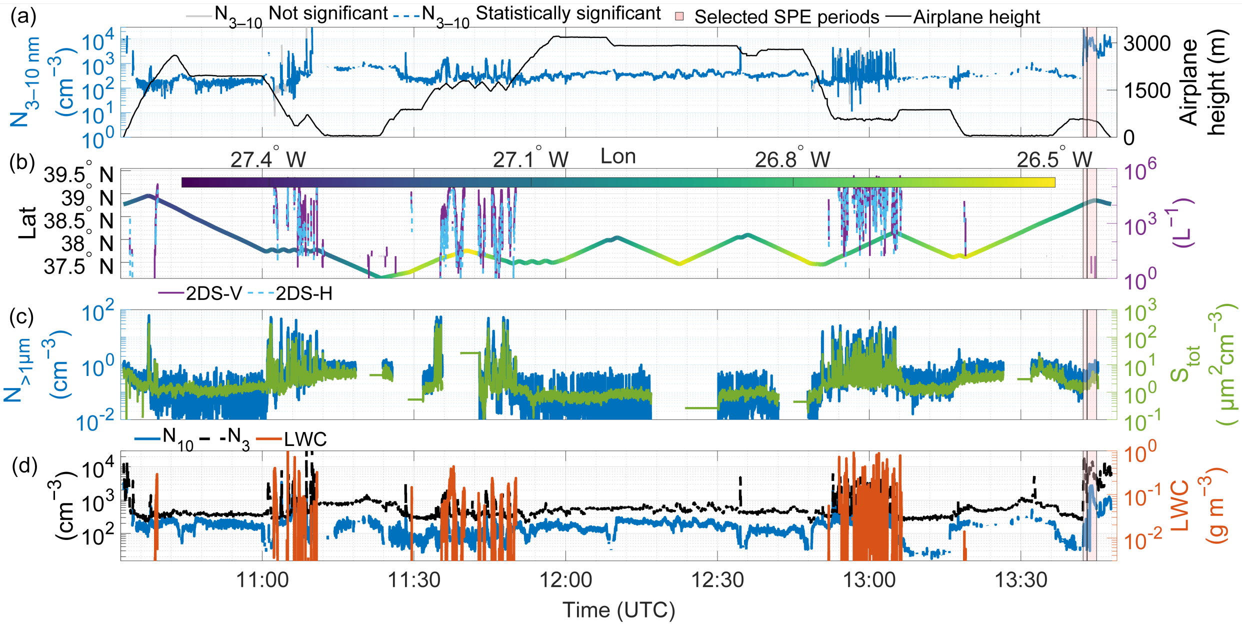

Figure S11. Multi-parameter time series analysis during the July 07, 2017 flight showing: (a) $N_{3\text{-}10}$ particle concentrations and aircraft altitude; (b) aircraft position (latitude and longitude) and drizzle number concentration; (c) supermicron particle concentration and total particle surface area (S_{tot}) (d) particle number concentrations (N_{10} and N_3) and liquid water content. Gaps in the time series indicate the missing data.

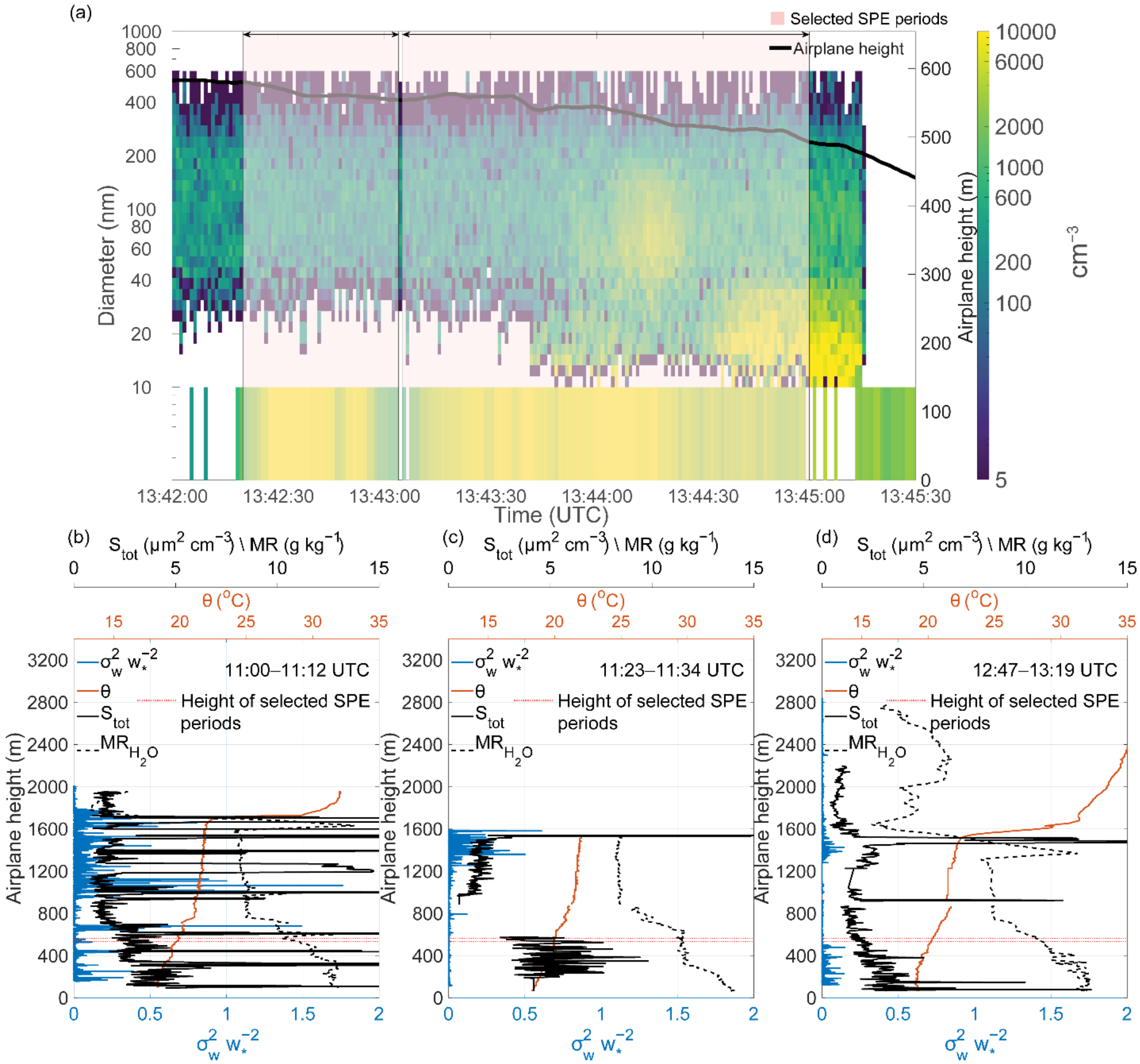

Figure S12. (a) Size-resolved particle number concentrations (10–600 nm) from FIMS as a function of time and altitude, with N_{3-10} concentrations shown in the lower strip. Pink shading indicates selected SPE periods. (b-d) Vertical profiles of potential temperature (θ), normalized vertical velocity variance ($\sigma_w^2\ w_*^{-2}$), total particle surface area (S_{tot}), and water vapor mixing ratio (MR_{H2O}) for three time periods nearest to the selected SPE periods: (b) 11:00–11:12 UTC, (c) 11:23–11:34 UTC, and (d) 12:47–13:19 UTC. Gaps in the time series indicate the missing data.

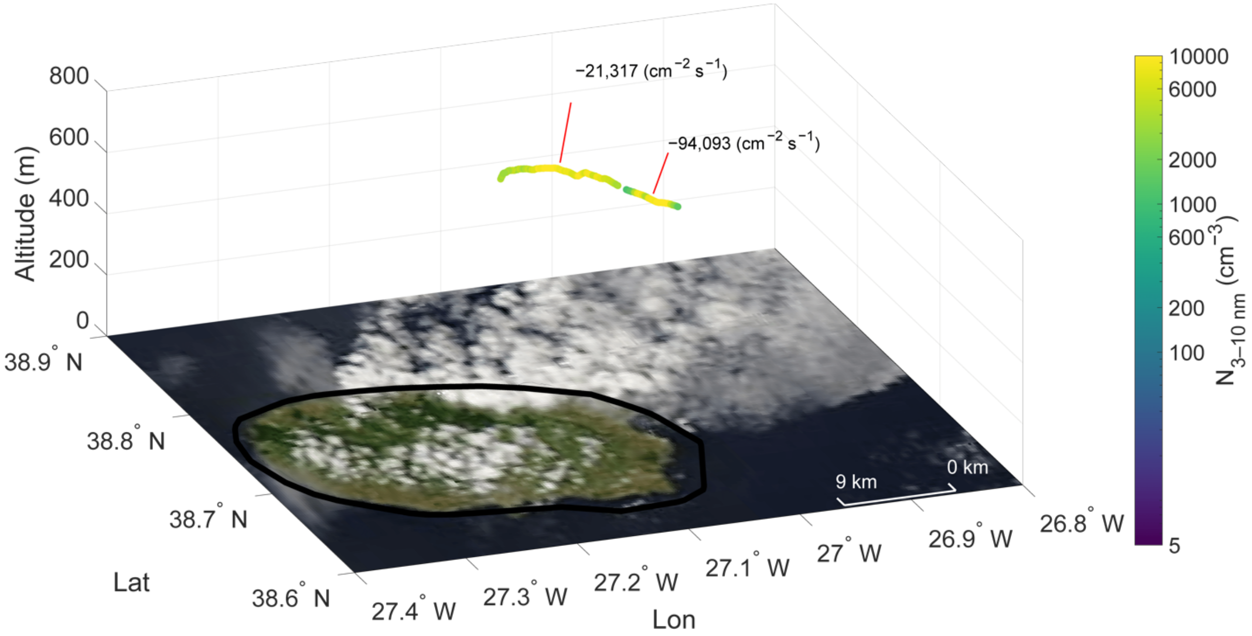

Figure S13. **Spatial distribution of N_{3-10} particle concentrations along the flight track at ~550 m altitude during the period highlighted in Figures S11 and S12. Calculated vertical turbulent fluxes are labeled at their respective measurement locations. Color scale indicates N_{3-10} particle number concentrations (cm^{-3}). The background shows a true-color satellite-corrected reflectance image from the overpass at 15:02 UTC with the ocean surface appearing dark and clouds appearing white, Credit: NASA Worldview Snapshots.**

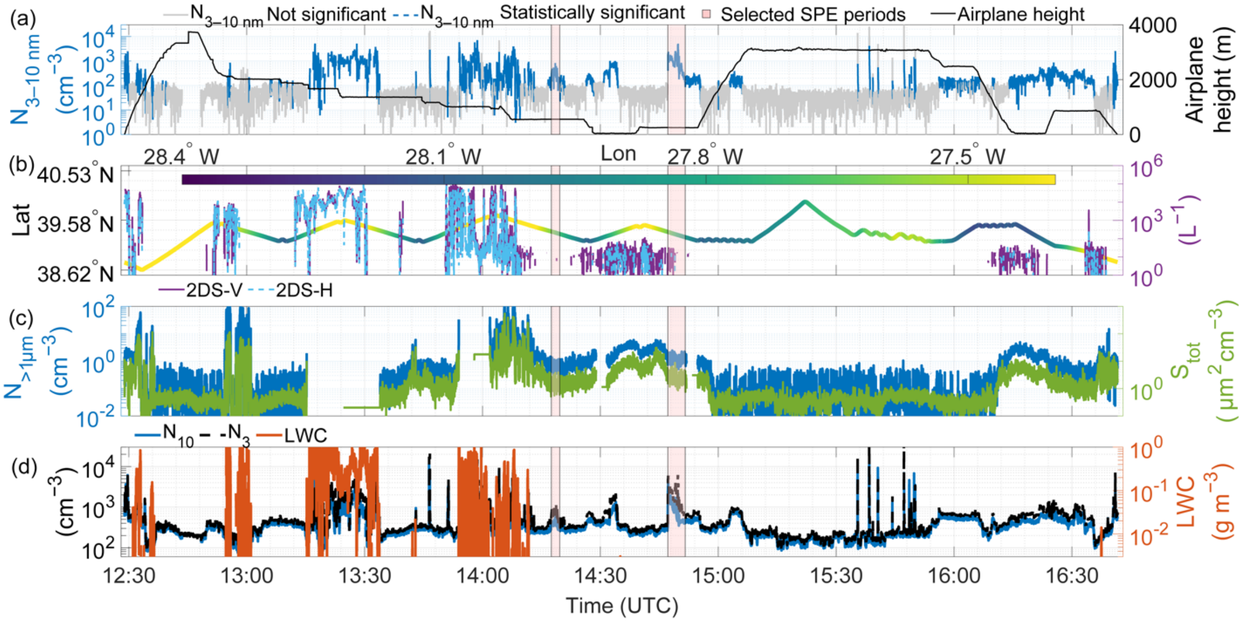

Figure S14. **Multi–parameter time series analysis during the February 18, 2018 flight showing: (a) $N_{3\text{-}10}$ particle concentrations and aircraft altitude; (b) aircraft position (latitude and longitude) and drizzle number concentration; (c) supermicron particle concentration and total particle surface area (S_{tot}) (d) particle number concentrations (N_{10} and N_3) and liquid water content. Gaps in the time series indicate the missing data.**

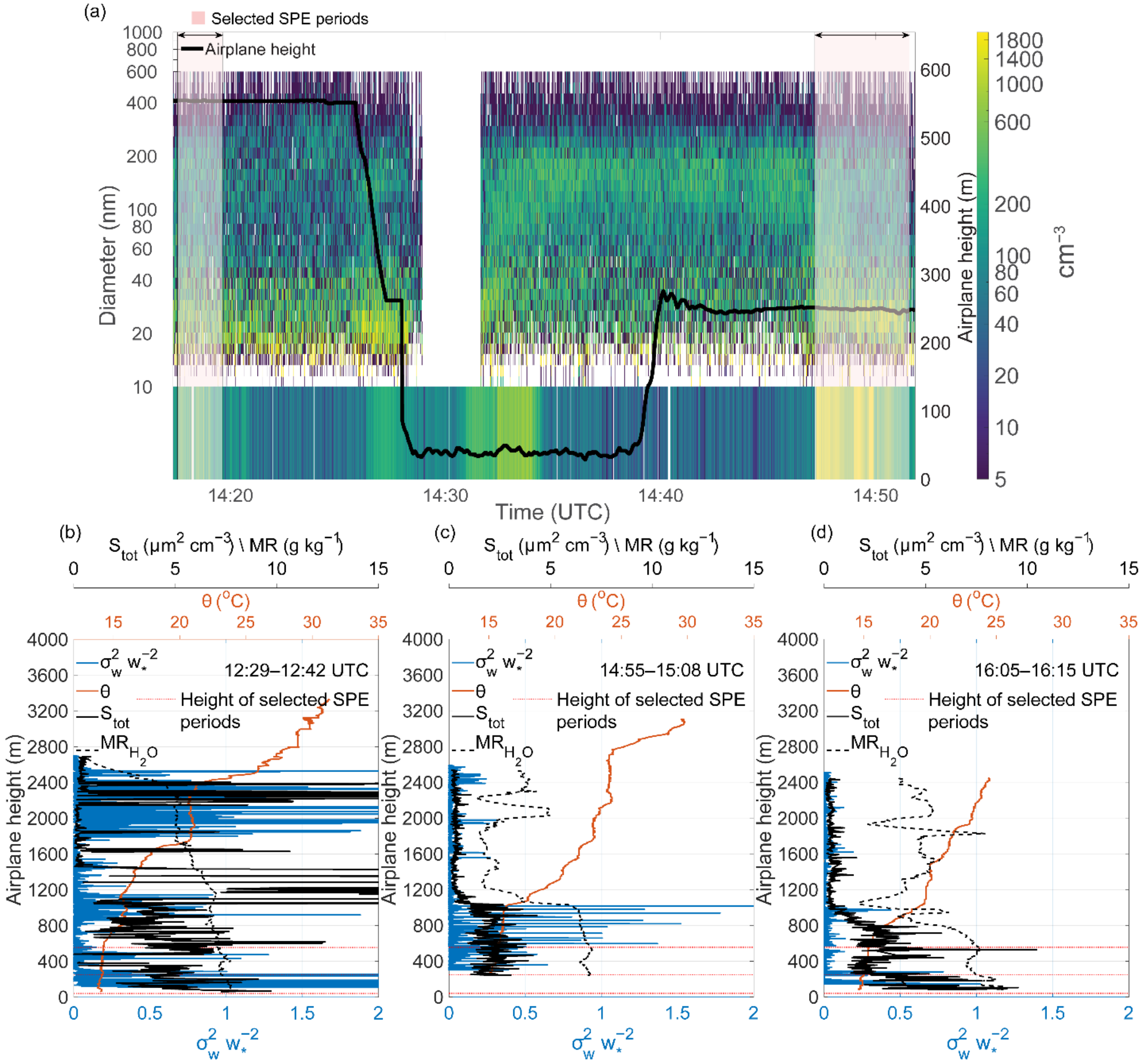

Figure S15. (a) Size-resolved particle number concentrations (10–600 nm) from FIMS as a function of time and altitude, with $N_{3\text{–}10}$ concentrations shown in the lower strip. Pink shading indicates selected SPE periods. (b-d) Vertical profiles of potential temperature (θ), normalized vertical velocity variance ($\sigma_w^2\, w_*^{-2}$), total particle surface area (S_{tot}), and water vapor mixing ratio (MR_{H2O}) for three time periods nearest to the selected SPE periods: (b) 12:29–12:42 UTC, (c) 14:55–15:08 UTC, and (d) 16:05–16:15 UTC. Gaps in the time series indicate the missing data.

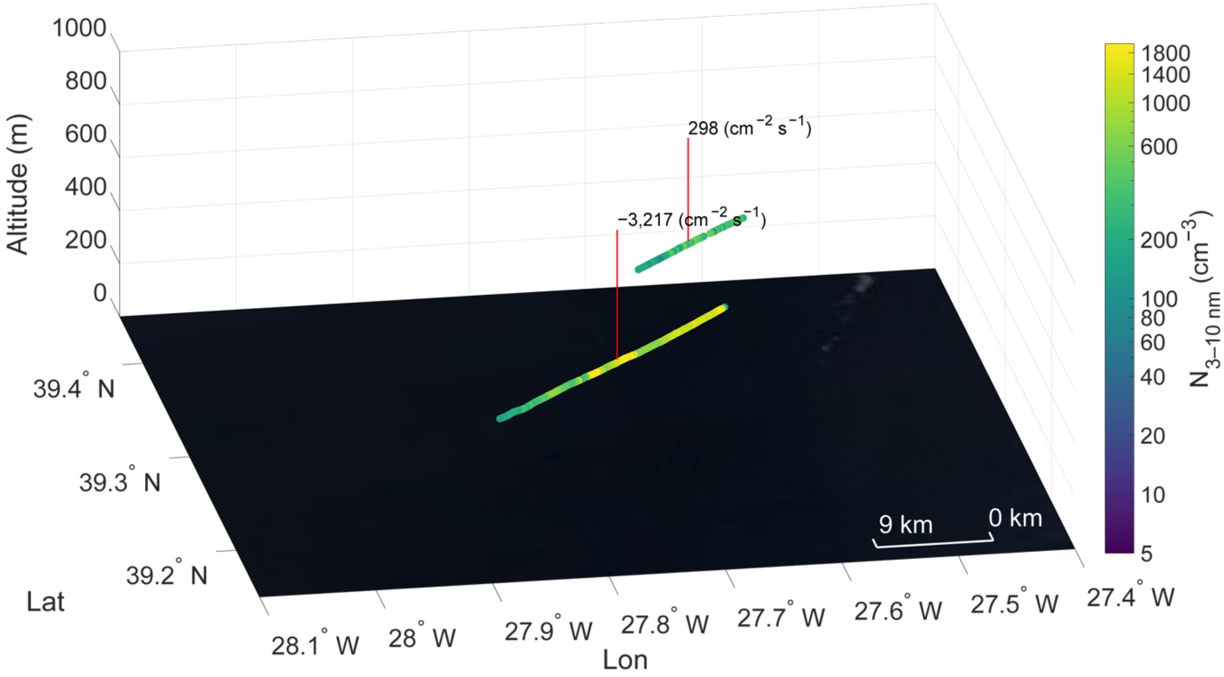

Figure S16. **Spatial distribution of N_{3-10} particle concentrations along the flight track at ~550 m and 250 m altitude respectively during the period highlighted in pink in Figures S14 and S15. Calculated vertical turbulent fluxes are labeled at their respective measurement locations. Color scale indicates N_{3-10} particle number concentrations (cm^{-3}). The background shows a true-color satellite-corrected reflectance image from the overpass at 14:50 UTC with the ocean surface appearing dark and clouds appearing white, Credit: NASA Worldview Snapshots.**

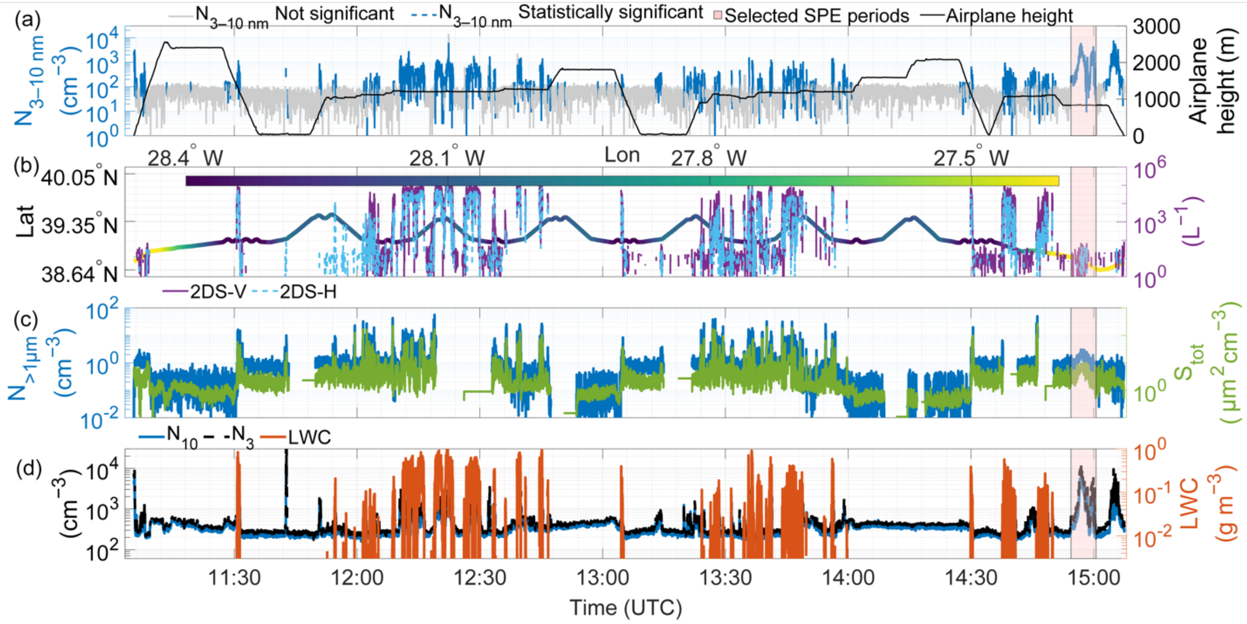

Figure S17. Multi–parameter time series analysis during the February 12, 2018 flight showing: (a) $N_{3\text{-}10}$ particle concentrations and aircraft altitude; (b) aircraft position (latitude and longitude) and drizzle number concentration; (c) supermicron particle concentration and total particle surface area (S_{tot}) (d) particle number concentrations (N_{10} and N_3) and liquid water content. Gaps in the time series indicate the missing data.

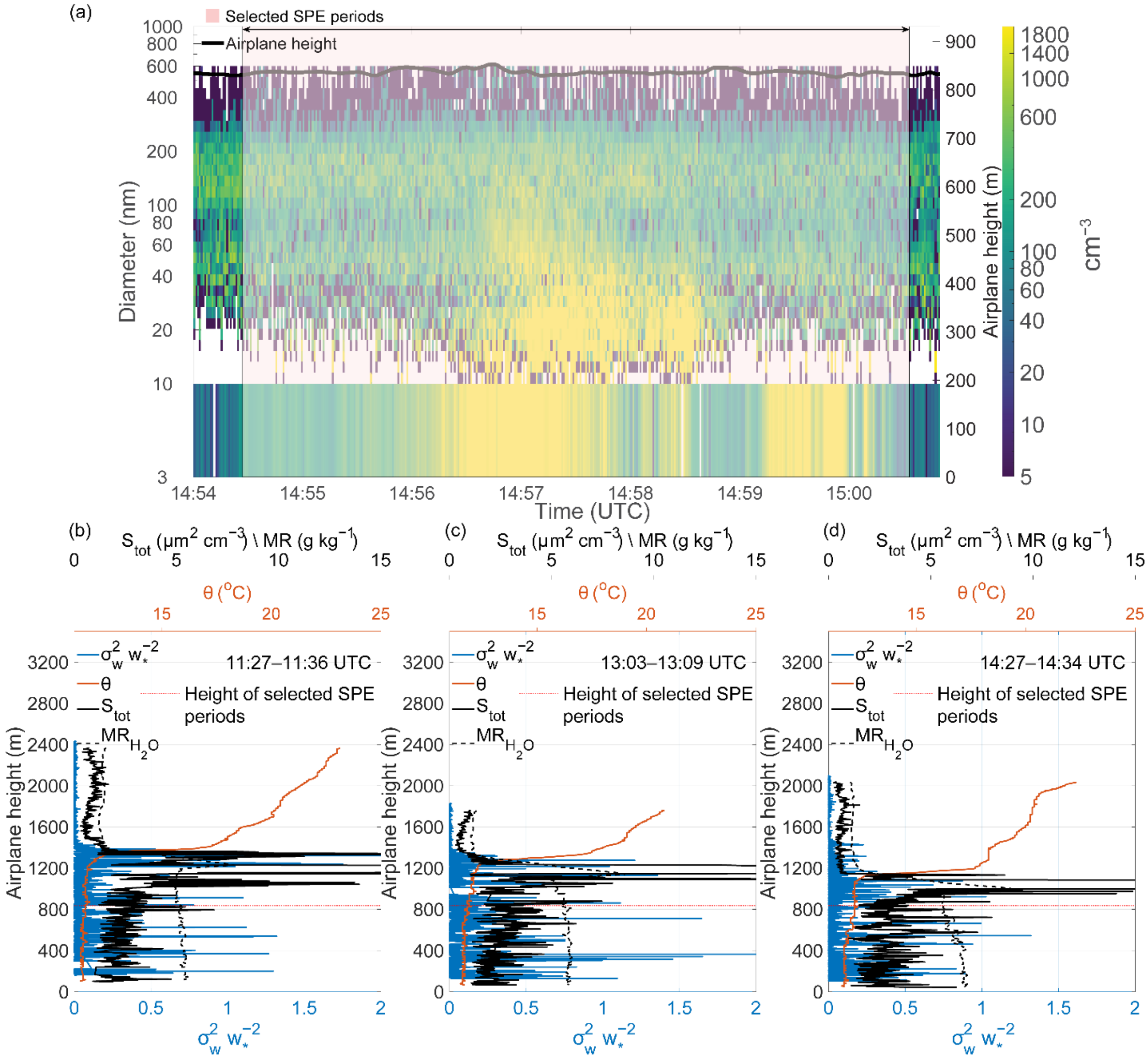

Figure S18. (a) Size-resolved particle number concentrations (10–600 nm) from FIMS as a function of time and altitude, with N_{3-10} concentrations shown in the lower strip. Pink shading indicates selected SPE periods. (b-d) Vertical profiles of potential temperature (θ), normalized vertical velocity variance ($\sigma_w^2\, w_*^{-2}$), total particle surface area (S_{tot}), and water vapor mixing ratio (MR_{H2O}) for three time periods nearest to the selected SPE periods: (b) 11:27–11:36 UTC, (c) 13:03–13:09 UTC, and (d) 14:27–14:34 UTC. Gaps in the time series indicate the missing data.

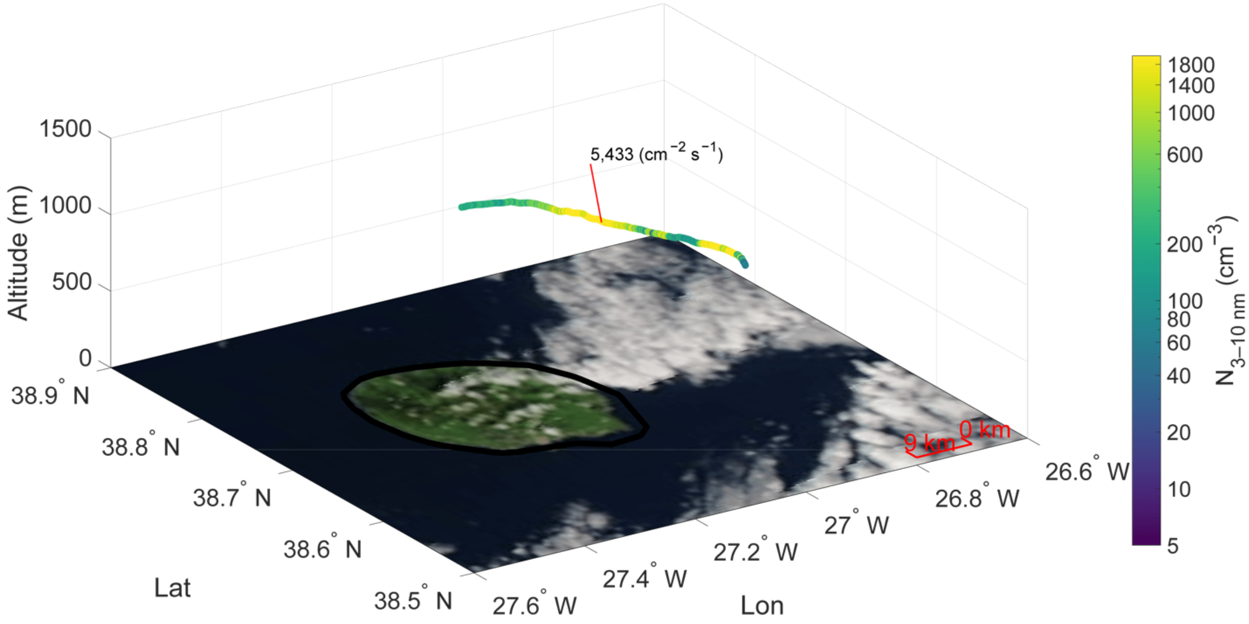

Figure S19. Spatial distribution of $N_{3\text{-}10}$ particle concentrations along the flight track at ~830 m altitude during the period highlighted in Figures S17 and S18. Calculated vertical turbulent fluxes are labeled at their respective measurement locations. Color scale indicates $N_{3–10}$ particle number concentrations (cm^{-3}). The background shows a true-color satellite-corrected reflectance image from the overpass at 15:27 UTC, with the ocean surface appearing dark and clouds appearing white, Credit: NASA Worldview Snapshots.